Title

Cell-type-specific origins of spinal rhythmicity at different locomotor speeds in larval zebrafish

Running title

Spinal rhythmogenesis during zebrafish swimming

Authors

Moneeza A. Agha[1,2], Sandeep Kishore[1], and David L. McLean[1,2,*]

Affiliations

[1] Department of Neurobiology, Northwestern University, Evanston, IL 60201

[2] Interdisciplinary Biological Sciences Graduate Program, Northwestern University, Evanston, IL 60201

* Correspondence: david-mclean@northwestern.edu

Conflict of interest

The authors declare no conflict of interest.

Acknowledgements

Support provided by NIH R21 NS125187 and NIH R21 NS125207.

Abstract

Different speeds of locomotion require heterogeneous spinal populations, but a common mode of rhythm generation is presumed to exist. Here, we explore the cellular versus synaptic origins of spinal rhythmicity at different speeds by performing electrophysiological recordings from premotor excitatory interneurons in larval zebrafish. Chx10-labeled V2a neurons are divided into at least two subtypes proposed to play distinct roles in timing and intensity control. Consistent with distinct rhythm generating and output patterning functions within the spinal V2a population, we find that one subtype is recruited exclusively at slow or fast speeds and exhibits intrinsic cellular properties suitable for rhythmogenesis at those speeds, while the other subtype is recruited more reliably at all speeds and lacks appropriate rhythmogenic cellular properties. Unexpectedly, however, phasic firing patterns during locomotion in rhythmogenic and non-rhythmogenic subtypes are best explained by distinct modes of synaptic inhibition linked to cell-type and speed. At fast speeds reciprocal inhibition in rhythmogenic V2a neurons supports phasic firing, while recurrent inhibition in non-rhythmogenic V2a neurons helps pattern motor output. In contrast, at slow speeds recurrent inhibition in rhythmogenic V2a neurons supports phasic firing, while non-rhythmogenic V2a neurons rely on reciprocal inhibition alone to pattern output. Our findings suggest cell-type-specific, not common, modes of rhythmogenesis generate and coordinate different speeds of locomotion.

Introduction (<5000)

All forms of vertebrate locomotion rely on rhythmic activity in muscles operating as functional antagonists (Grillner, 1985). For instance, swimming in fishes relies on left-right alternation of axial muscles across the body, while walking in mammals relies on flexor-extensor alternation along it. A landmark hypothesis posed over a century ago argued for corresponding excitatory 'half-centers' within spinal cord (e.g., left-right or flexor-extensor), with reciprocal, feedforward inhibition between half-centers generating rhythmic output (Brown, 1911). Since then reciprocal inhibition has been relegated to patterning activity between so-called 'unit burst generators' capable of rhythmogenesis via recurrent, feedback excitatory connections (Grillner and Kozlov, 2021).

The idea of solitary unit burst generators reliant on recurrent connectivity disconnects rhythmogenesis from activity in other unit burst generators, which helps explain the flexible patterns of coordination necessary to effectively navigate through unpredictable environments. For example, simulations adjusting the synaptic coupling strength between segmental axial unit burst generators can explain changes in the speed and direction of swimming in lampreys (Kozlov et al., 2009). Likewise, simulations altering the synaptic coupling between segmental limb unit burst generators can replicate different speeds and gaits of locomotion in cats (Grillner, 1981).

Another theory explaining speed-dependent changes in coordination stratifies 'rhythm' and 'pattern' control (McCrea and Rybak, 2008), where populations of interneurons generating higher or lower frequency rhythms feed into separate populations coordinating distinct patterns of motor output (Ausborn et al., 2019). In support, studies in zebrafish and mice suggest separate spinal populations are active at different locomotor speeds (McLean et al., 2008; Talpalar et al., 2013; Satou et al., 2020; Picton et al., 2022). Critically, however, a common mode of rhythmogenesis is presumed to exist at all speeds regardless of topological framework, reliant on either cellular properties or synaptic drive (Guertin, 2009; Brocard et al., 2010; Ryczko et al., 2010; Ziskind-Conhaim and Hochman, 2017; El Manira, 2023).

Here, we have explored the origins of spinal rhythmogenesis at different speeds using the larval zebrafish model system, where it is possible to link the identity, physiology and connectivity of interneurons to their recruitment patterns at different speeds of locomotion. Like all fish, larval zebrafish generate two basic modes of forward swimming or 'gaits' (Di Santo et al., 2021). Anguilliform mode is typically reserved for escaping predators and uses higher frequency/amplitude oscillations of the trunk, while carangiform mode utilizes lower frequency/amplitude oscillations of the tail for exploration and pursuing prey (Budick and O'Malley, 2000; Muller and van Leeuwen, 2004; Thorsen et al., 2004; Patterson et al., 2013; Bhattacharyya et al., 2021).

Swimming at different speeds is generated by axial motor neurons organized into fast, slow and intermediate units distinguished by birth order (Myers et al., 1986), size (McLean et al., 2007), relative innervation of fast and slow muscle fibers (Bello-Rojas et al., 2019), and molecular signatures (D'Elia et al., 2023). Current-clamp and voltage-clamp recordings from motor neurons have revealed differences in

rhythmogenic cellular properties and synaptic drive between the different types (Menelaou and McLean, 2012; Kishore et al., 2014), suggesting different forms of rhythmogenesis could be responsible for different speeds of locomotion. To test this idea, we performed current-clamp and voltage-clamp recordings from Chx10-labeled spinal V2a interneurons, which provide a major source of phasic premotor excitation during locomotion in zebrafish and mice (McLean and Dougherty, 2015).

We find that V2a neurons sort into rhythm-generating and pattern-forming subtypes based on distinct cellular properties linked to distinct patterns of recruitment and synaptic drive. Critically, among V2a neurons that qualify as rhythm-generating, reciprocal inhibition originating from contralateral sources supports phasic firing patterns at fast speeds, while recurrent inhibition from ipsilateral sources supports phasic firing patterns at slow speeds. For V2a neurons considered pattern-forming, the opposite is true – recurrent inhibition supports phasic firing at fast speeds and reciprocal inhibition at slow speeds. Ultimately, our findings reveal unexpected cell-type-specific and speed-dependent complexity in the mechanisms of spinal rhythmogenesis underlying locomotion.

Results

Identifying V2a neurons for recordings during 'fictive' escape swimming

From our previous work studying V2a neurons in larval zebrafish we know they are organized into: 1) fast and slow subtypes based on dorso-ventral soma position and birth order (McLean et al., 2007; McLean et al., 2008; McLean and Fetcho, 2009), and 2) distinct subtypes that provide stronger direct versus indirect control of motor neuron recruitment (Menelaou et al., 2014; Menelaou and McLean, 2019). Specifically, V2a neurons with descending axons (V2a-D) provide stronger inputs to other premotor interneurons, while V2a neurons with bifurcating axons (V2a-B) provide stronger inputs to motor neurons (Menelaou and McLean, 2019), in line with differential rhythm and pattern control (Feldman, 1986). However, we do not know if the same mechanisms of rhythmogenesis shape the phasic activation of distinct V2a types at different speeds.

To record from distinct types of V2a neurons, we targeted GFP-positive neurons located at midbody in the Tg(Chx10:GFP) line (Fig. 1A,B)(Kimura et al., 2006), since midbody neurons would be recruited during both fast anguilliform and slow carangiform modes (Muller and van Leeuwen, 2004; Thorsen et al., 2004). V2a-D and V2a-B neurons recruited at fast speeds can be distinguished by levels of Chx10 expression in transgenic lines (Menelaou and McLean, 2019), as reported in mice (Hayashi et al., 2018). To get a better sense of differences in the number and spatial distribution of distinct types, we split GFP-positive neurons into two categories based on a bimodal distribution of fluorescence intensity and normalized their soma positions to dorso-ventral and medio-lateral axes in the spinal cord. Larger, dimmer V2a neurons intermingled with smaller, brighter neurons along the dorso-ventral axis (Fig. 1C, *left*), but occupied more lateral positions (Fig. 1C, *right*). Statistical analysis confirmed these observations, with no significant difference in either dorso-ventral distribution (Fig. 1D, *left*) or number per segment between the low or high GFP-positive types (Fig. 1D, *right*), but a significant difference in mediolateral position (Fig. 1E).

105 To evaluate firing patterns and synaptic drive responsible for rhythmogenesis in different types, we
106 recorded from V2a neurons during 'fictive' swimming evoked by a mild electrical shock, while
107 simultaneously monitoring rhythmic motor output using ventral rootlet recordings (Fig. 1F). During real
108 swimming, escape responses decelerate, beginning in fast anguilliform mode and ending in slow
109 carangiform mode (McLean et al., 2008; McLean and Fetcho, 2009). Plots of ventral rootlet burst
110 frequencies with time confirm this pattern during 'fictive' escape responses, where we observe the highest
111 frequencies at the beginning of the swim episode immediately following the stimulus (Fig. 1G, *left*). Notably,
112 zebrafish swimming is episodic (McHenry and Lauder, 2006; Soto and McHenry, 2020) and so it can
113 continue intermittently after the initial escape swim episode. Subsequent episodes (swim 2+) rarely
114 exceeded peak firing frequencies observed in the first stimulus-evoked episode (> 60 Hz in swim 1) and
115 there was more variability in frequency (Fig. 1G, *right*). For purposes of analysis we pooled data from the
116 first (swim 1) and subsequent (swim 2+) episodes to capture as broad a frequency range as possible.

117 Thus, different types of V2a neurons can be easily distinguished for targeting purposes and we can assess
118 their firing and synaptic drive during fast anguilliform and slow carangiform modes distinguished by
119 frequency and temporal sequence within fictive escape swim episodes. This set the stage for asking if the
120 same mechanism of rhythmogenesis drives the phasic activation of distinct V2a types at different speeds.

121 *Differences in intrinsic rhythmogenesis related to V2a neuron type*

122 Rhythmogenesis can originate from cellular properties of synaptic drive or some combination of the two
123 (Marder and Calabrese, 1996; Marder and Bucher, 2001). In theory, neurons that are intrinsically
124 rhythmogenic can create patterned outputs from unpatterned inputs. Thus, to explore the intrinsic
125 rhythmicity of V2a neurons we performed whole-cell current-clamp recordings from high and low GFP-
126 positive V2a neurons and tested their firing responses to stable current steps. By including dye in our
127 recording pipette, we confirmed post-hoc that high GFP neurons were V2a-Ds and low GFP neurons were
128 V2a-Bs (Fig. 2A). Differences in sizes and dorso-ventral distributions of V2a-D and V2a-B neurons in our
129 current-clamp dataset (n = 41) were consistent with our analysis of high and low GFP neurons in stable
130 lines (Fig. 2B, *left*). Also, measurements of input resistance and rheobase current were consistent with
131 differences in sizes and excitability between the two types (Fig. 2C, *left*). Thus, we were confident of a
132 sufficient sampling of V2a neurons to explore differences in rhythmogenic capacity related to type and
133 recruitment order.

134 V2a-D neurons with 'tonic' responses and V2a-B neurons with higher frequency 'chattering' ones were
135 distributed dorsally and had the lowest input resistances in their respective types (Fig. 2B-E). In tonic V2a-
136 Ds, firing above rheobase current was observed consistently throughout the current step (Fig. 2E, *top*), with
137 instantaneous spike rates increasing linearly with increasing current, starting around 40 Hz and reaching
138 200 Hz (Fig. 2D). In chattering V2a-Bs, firing above rheobase current was intermittent throughout the step
139 (Fig. 2F, *top*), with instantaneous rates starting around 200 Hz and reaching 600 Hz (Fig. 2D). These

observations are consistent with previous recordings from fast V2a-D and V2a-B neurons (Menelaou and McLean, 2019).

On the other hand, V2a-D and V2a-B neurons with 'burst' responses were distributed ventrally and had the highest input resistances within their respective types (Fig. 2B-E). In bursting V2a neurons, firing above rheobase was characterized by higher frequency spikes superimposed on lower frequency membrane potential oscillations (Fig. 2E-F, *bottom*). While the frequency of the slower oscillations increased with current (Fig. 2E-F, *bottom*), instantaneous spike rates were already close to peak values at rheobase (500-600 Hz; Fig. 2D). Beyond 2-3x rheobase current, slower oscillations were no longer obvious and the firing pattern more closely resembled the chattering one (data not shown), as observed previously for motor neurons (Menelaou and McLean, 2012).

Next, we compared the firing properties of distinct types of V2a neurons to their recruitment patterns during fictive escape swimming. As expected (Menelaou and McLean, 2019), both tonic V2a-D and chattering V2a-B neurons were recruited at the beginning of the episode at median swim frequencies above 30 Hz (Fig. 2G-H), consistent with recruitment during fast anguilliform mode (Thorsen et al., 2004; McLean et al., 2008; McLean and Fetcho, 2009). In contrast, burst V2a-Ds fired more reliably at the end of the episode at median frequencies that rarely exceeded 30 Hz (Fig. 2G-H), consistent with participation in slow carangiform mode (Thorsen et al., 2004; McLean et al., 2008; McLean and Fetcho, 2009). Burst V2a-Bs were recruited just below 30 Hz, and fired more reliably throughout the episode and over a broader frequency range (Fig. 2G-H). A comparison between the step firing and swim firing patterns among V2a-D neurons revealed a remarkable correspondence (Fig. 2G), with median spike frequencies (tonic) or oscillation frequencies (burst) overlapping median recruitment frequencies during swimming (Fig. 2I, *left*). However, the link between step firing and swim firing patterns was less obvious for V2a-B neurons (Fig. 2G). For example, while bursting V2a-B neurons recruited at swim frequencies exceeding 60 Hz had higher frequency oscillations, step bursting rarely exceeded 20 Hz (Fig. 2I, *right*).

Thus, distinct electrophysiological properties define distinct V2a types recruited at different speeds and V2a-D neurons are better suited to providing intrinsic rhythmogenic activity during fast and slow swimming modes. This is consistent with their proposed rhythm-generating and pattern-forming roles (Menelaou and McLean, 2019), and suggests V2a-B neurons rely more on rhythmic synaptic drive to shape their phasic firing patterns during swimming.

Both types of V2a neuron operate at slow and fast speeds

Our current-clamp data suggest that different types would rely differently on cellular properties versus synaptic drive for rhythmogenesis. To test this idea more directly, we performed voltage-clamp recordings during fictive escape swimming. To more effectively isolate synaptic currents, we included cesium in the patch solution. Since this blocks voltage-gated channels and spiking, we needed to classify fast and slow V2a-D and V2a-B neurons subtypes by first monitoring spikes in cell-attached mode. Consistent with our current-clamp recordings, in our voltage-clamp dataset (n = 39) we found V2a-D and V2a-B neurons that

fired at the beginning of the escape episode or nearer the end (Fig. 3a). V2a-D neurons fired more sparsely (Fig. 3A, *left*) and were divided into two distinct groups: 1) neurons that fired exclusively at the beginning of the episode at median swim frequencies exceeding 40 Hz, and 2) neurons that fired later on in the episode at median swim frequencies rarely exceeding 30 Hz (Fig. 3B,*left*; 3C). On the other hand, V2a-B neurons fired more reliably (Fig. 3A, *right*) and median values were more continuous, making it more difficult to group neurons based on location within the episode (Fig. 3B, *right*) or swim frequency (Fig. 3D).

To better segregate both types of V2a neurons based on speed, we used the frequency-dependent transition between anguilliform and carangiform modes to define V2a neurons recruited more reliably below 35 Hz as 'slow' and V2a neurons recruited more reliably above 35 Hz as 'fast' (Fig. 4A). Consistent with our current-clamp recordings, slow V2a-D and V2a-B neurons in our voltage-clamp recordings were more ventrally distributed with higher resistances than fast V2a-D and V2a-B neurons (Fig. 4B). A closer examination of spike timing relative to individual ventral rootlet bursts revealed median spike distributions in advance of the center of the motor burst, as expected for premotor excitatory interneurons involved in rhythmogenesis (Fig. 4C). Plots of spike densities normalized to center burst revealed that V2a-B neurons begin to fire slightly in advance of V2a-D neurons (Fig. 4D), consistent with differences in membrane resistance related to size, where neurons with faster time constants respond more quickly to synchronous inputs (Menelaou and McLean, 2019).

Next, to explore recruitment probability as a function of speed in more depth we divided the full range of fictive swimming frequencies into four bins distributed around 35 Hz. For V2a-D neurons, fast neurons were rarely recruited below 35 Hz and increased to a maximum of 50% recruitment reliability per motor burst above 35 Hz (Fig. 4E, *top left*). Similarly, slow V2a-D neurons did not exceed 50% recruitment reliability per motor burst below 35 Hz and rarely fired above it (Fig. 4E, *top right*). When collapsed into two bins below and above 35 Hz, these differences in recruitment probability were significant (Fig. 4F, *top*). For V2a-B neurons, fast neurons fired more reliably below 35Hz than fast V2a-Ds and increased to 100% recruitment reliability per motor burst above 35 Hz (Fig. 4E, *bottom left*). Similarly, slow V2a-B neurons fired more reliably above 35 Hz than slow V2a-Ds, and at 100% reliability below it (Fig. 4E, *bottom right*). Binning of recruitment among V2a-Bs revealed significant differences related to speed among the fast subtypes only (Fig. 4F, *bottom*). Among the slow V2a-Bs, decreases in recruitment reliability were observed in the majority of neurons (n = 5 of 6), however the difference was not significant when pooled (Wilcoxon signed-rank test, V=20, p=0.0625, n = 6).

In further support of the speed-based modular organization of V2a neurons, in slow types higher instantaneous spike rates were observed at lower burst frequencies, while in fast types higher spike rates were observed at higher burst frequencies (Fig. 4G, *top*). Critically, spike rates observed during fictive swimming overlap with those observed during current steps between 1-2x rheobase, ranging from in 200-600 Hz (Fig. 4H, *top*), with the fastest spike rates observed in fast V2a-B neurons. This suggests that the firing patterns observed during current injections between 1-2x rheobase are functionally relevant. When

212 we measured spike numbers per burst, lower numbers were consistently observed at higher burst
213 frequencies regardless of type or speed class (Fig. 4G, *bottom*) consistent with less time to spike during
214 shorter cycle periods. In addition, V2a-B neurons fired significantly more spikes per burst than V2a-Ds on
215 average (Fig. 4H, *bottom*), consistent with their higher recruitment probabilities.

216 Thus, within our voltage-clamp dataset we have V2a-D and V2a-B neurons operating during anguilliform
217 and carangiform swimming modes. While V2a-D neurons fire more sparsely and in a stricter modular
218 fashion, V2a-B neurons fire more reliably and over a broader range of frequencies, consistent with
219 occupation of a pattern forming layer downstream of distinct fast and slow rhythmic signals.

220 *Differences in the levels of synaptic drive mirror differences in speed modularity*

221 To get a better sense of the relative segregation of synaptic inputs to V2a-D and V2a-B neurons based on
222 speed, we first focused on the maximum amplitude of excitatory and inhibitory currents recorded during
223 fictive escape swimming. Clamping V2a neurons at a potential to isolate excitatory post-synaptic currents
224 (EPSCs) revealed faster time course, compound EPSCs superimposed on a slower, tonic inward current
225 (Fig. 5A,B). While tonic excitation was observed the entirety of the episode, fast V2a-Ds received compound
226 EPSCs exclusively during high frequency swimming at the beginning (Fig. 5A, *top*), while slow V2a-D's
227 received compound EPSCs exclusively during slower swimming later in the episode (Fig. 5A, *bottom*),
228 consistent with their recruitment patterns. A similar pattern was observed among V2a-Bs, however
229 compound EPSCs were observed over a broader range of frequencies (Fig. 5B), also consistent with their
230 recruitment patterns. We also noted differences in maximum levels of current related to type. When we
231 plotted maximum current (tonic current + compound EPSCs) versus input resistance, we observed a
232 significant negative correlation, with lower resistance V2a-Bs receiving orders of magnitude more
233 excitation than higher resistance V2a-Ds (Fig. 5C). This is consistent with peak excitatory drive normalized
234 to cellular excitability, as reported previously (Menelaou et al., 2022).

235 Next, clamping V2a neurons at a potential to isolate inhibitory post-synaptic currents (IPSCs) revealed
236 faster time course compound IPSCs superimposed on a slower, tonic outward current (Fig. 5D-E). In all
237 V2a types tonic inhibition persisted the entirety of the episode and compound IPSCs were larger at higher
238 frequencies near the beginning (Fig. 5D-E). Like excitation, plots of maximum current (tonic current +
239 compound IPSCs) revealed a significant negative correlation between inhibitory current and input
240 resistance (Fig. 5F), meaning that peak inhibitory drive is also normalized to cellular excitability. Given
241 these large differences in maximum current values, to compare frequency-dependent changes in excitation
242 and inhibition, we normalized the currents for each cycle to the maximum currents for the neuron (Fig. 5C,
243 5F). So, maximum EPSCs or IPSCs in a given cycle are expressed as a percentage of the maximum value in
244 all cycles at any speed.

245 For fast V2a-D and V2a-B neurons, maximum excitatory drive increased with increasing frequency (Fig.
246 5G, *left*). Differences in maximum excitation were significant for both types when data were pooled (Fig.
247 5H), consistent with their recruitment patterns (Fig. 4F). Inhibition also followed the same pattern for fast

248 V2a neurons (Fig. 5I, *left*), significantly increasing at fast speeds (Fig. 5J). For slow V2a-D neurons
249 excitation was significantly lower at higher frequencies (Fig. 5G, *top right*; 5H, *top*) and inhibition was
250 significantly higher (Fig. 5I, *top right*; 5J, *top*). However, for slow V2a-B neurons neither excitation (Fig.
251 5G, *bottom right*; 5H, *bottom*) nor inhibition (Fig. 5I, *bottom right*; 5J, *bottom*) changed significantly when
252 pooled, despite the decreases in excitation (n = 4 of 6) and increases in inhibition (n = 5 of 6) in the majority
253 of neurons. These patterns of excitation and inhibition are consistent with recruitment patterns, where slow
254 V2a-D neurons are silenced at fast speeds and slow V2a-B neurons are recruited albeit with lower reliability
255 (Fig. 4F).

256 While the increase in inhibition at fast speeds to slow V2a neurons makes sense in terms of their
257 disengagement during fast anguilliform mode (McLean et al., 2008), the increase in inhibition to fast V2a
258 neurons clearly does not have a similar impact, despite being normalized to excitability. Indeed, when we
259 compared the maximum excitation and inhibition to V2a-Ds (Fig. 5K) and V2a-Bs (Fig. 5L), maximum
260 inhibition was orders of magnitude larger than maximum inhibition. Even when controlling for differences
261 in driving forces experienced at resting potentials, it would be difficult for V2a neurons to fire if excitation
262 and inhibition arrived concurrently.

263 Thus, measurements of maximum levels of excitatory and inhibitory drive that include fast phasic and
264 slower tonic components are consistent with recruitment patterns. These data also suggest the timing of
265 inhibition plays a critical role in shaping the rhythmic output of V2a neurons more broadly.

266 *Differences in the timing of synaptic drive better explain rhythmic V2a recruitment*

267 To compare the timing of compound EPSCs and IPSCs we normalized the amplitude to the maximum (1)
268 and minimum (0) values for that cycle and normalized the timing to the phase of the swim cycle, with the
269 centers of two successive motor bursts demarcating phase 0 and 1 (Fig. 6A). To simplify comparisons
270 between peaks in excitation and troughs in inhibition, we inverted the sign of excitation. By convention,
271 synaptic currents arriving between 0.75 – 0.25 are described as 'in-phase' with local motor output, while
272 currents arriving 0.25 – 0.75 are described as 'anti-phase'. In fish, in-phase currents are assumed to arise
273 from recurrent sources on the ipsilateral side, while anti-phase currents arise from the reciprocal sources
274 on the contralateral side. This means that differences in the timing of peaks of excitation and inhibition can
275 be used to draw inferences about patterns of connectivity along and across the body.

276 First, to assess differences in the timing of compound EPSCs and IPSCs, we low pass filtered the raw current
277 trace to identify peaks in-phase and anti-phase (Fig. 6A, *black dots*), which were then plotted on a circular
278 axis and compared to cell-attached spiking activity (Fig. 6B-C). For all V2a neurons, spikes were exclusively
279 distributed in-phase with local motor output (Fig. 6B, *left*; 6C, *left*), however there were type-specific
280 differences in the distributions of peak excitation and inhibition.

281 For fast V2a-Ds phasic excitation began early in anti-phase, with a peak distribution in-phase coinciding
282 with a dip in phasic inhibition and spiking activity (Fig. 6B, *top*). Phasic inhibition was also broadly

283 distributed, with peak values in anti-phase (Fig. 6B, *top right*). For slow V2a-Ds, phasic excitation was also
284 phase advanced relative to spiking activity (Fig. 6B, *bottom*), with peaks obvious earlier in anti-phase (Fig
285 6B, *bottom right*). Unlike fast V2a-Ds, however, there were two clear peaks in phasic inhibition, one
286 immediately trailing in-phase excitation (Fig. 6B, *bottom right arrow*) and one peaking anti-phase.
287 Notably, the presence of in-phase inhibition was also associated with a more coherent distribution of spikes
288 in the slow V2a-Ds (c.f., Fig. 6B, *left*). For fast and slow V2a-Bs, phasic excitation was found exclusively in-
289 phase, coincided well with spike distributions and was more coherent than V2a-Ds (Fig. 6C), consistent
290 with the idea they are downstream of V2a-D neurons. Remarkably, however, the pattern of phasic inhibition
291 was inverted, such that fast V2a-Bs received peaks in-phase and anti-phase (Fig. 6C, *top right arrow*), while
292 slow V2a-Bs received predominantly anti-phase inhibition (Fig. 6C, *bottom right*). Differences in the
293 predominance of in-phase inhibition between V2a-B types were also associated with differences in the
294 coherence of spiking activity (Fig. 6C, *left*), as observed for V2a-D types (Fig. 6B, *left*).

295 Next, to get a better sense of how patterns of phasic excitation and inhibition differ within types at different
296 speeds, we binned the data by frequency as above and examined averages of normalized raw current traces.
297 Among the V2a-Ds, fast subtypes exhibited reciprocal inhibition at all frequencies, with phasic peaks in
298 excitation and inhibition most obvious at higher frequencies coincident with spiking activity (Fig. 6D, *top*).
299 Among slow V2a-Ds, coherent peaks in reciprocal and recurrent inhibition were most obvious at slow
300 speeds coincident with phasic excitation and spiking behavior (Fig. 6D, *bottom*). Among the V2a-Bs,
301 patterns of reciprocal and recurrent inhibition were consistent across all speed bins, with peaks in phasic
302 excitation and dips in phasic inhibition coincident with spiking activity (Fig. 6E).

303 Thus, despite differences in cellular rhythmogenic capacity, these observations suggest all types of V2a
304 neurons rely on phasic excitation and inhibition to sculpt their rhythmic firing behavior during swimming.
305 Peaks in phasic excitation arrive earlier among V2a-D neurons, consistent with their hierarchical
306 positioning upstream from V2a-B neurons, and the relative coherence of phasic excitatory and inhibitory
307 drive at different frequencies is consistent with speed modularity in this population. Among V2a-B neurons,
308 the coherence of phasic excitatory and inhibitory drive over the entire frequency range is consistent with a
309 role integrating inputs from the different speed modules. Critically, these data also suggest reciprocal
310 inhibition plays a key role in rhythmogenesis at fast speeds, while recurrent inhibition plays a more
311 dominant role in rhythmogenesis at slow speeds.

312 **Discussion**

313 Our work was motivated by the opaque origins of spinal rhythmicity at different locomotor speeds and the
314 potential for zebrafish to clarify this fundamental issue. By recording from different subtypes of V2a
315 neurons during slow and fast fictive swimming we have, for the first time, linked cellular and synaptic
316 properties to recruitment patterns over nearly a full operational range of locomotion. First, our recordings
317 reveal that all V2a neurons demonstrate some form of rhythmicity in response to current steps. The idea
318 that different types of V2a interneurons exhibit different firing properties is not unexpected (Dougherty

319 and Kiehn, 2010; Zhong et al., 2010; Menelaou and McLean, 2019; Song et al., 2020). However, thanks to
320 our ability to link cellular properties to natural recruitment patterns we reveal V2a-Ds alone would qualify
321 as 'pacemakers' (Marder and Calabrese, 1996; Marder and Bucher, 2001), with speed-dependent
322 differences in intrinsic firing mode within V2a-Ds. Specifically, V2a-D neurons recruited at swim
323 frequencies below ~40 Hz during carangiform swimming generate intrinsic bursting at those frequencies,
324 while V2a-D neurons recruited at frequencies above ~40 Hz during anguilliform swimming generate tonic
325 firing at those frequencies. In V2a-B neurons, chattering and bursting properties in response to current
326 steps do not reflect their natural firing patterns during swimming, and so we expected they would rely more
327 on pacemaking inputs from V2a-Ds to shape their rhythmicity.

328 Surprisingly, however, we found that both V2a-Ds and V2a-Bs receive phasic excitatory input, and so
329 synaptic signals are already rhythmic by the time they arrive. This could be because our recordings were
330 performed at midbody and so rhythms are generated by more rostral V2a-Ds with identical cellular
331 properties. Optogenetic and lesion studies support a rostral bias in spinal rhythmicity in larval zebrafish
332 (Wiggin et al., 2012; Kimura et al., 2013), consistent with studies of spinal locomotor networks in lampreys
333 and tadpoles, where neurons nearer the hindbrain/spinal cord boundary have a higher capacity for
334 rhythmogenesis (Li et al., 2010; Buchanan, 2018). On the other hand, bursting properties could serve as a
335 source of amplification for synaptic inputs to ensure reliable recruitment of rhythmogenic neurons or to
336 ensure rhythmogenesis in cases where synaptic drive fails or the spinal cord is damaged (Messina et al.,
337 2017; Parker, 2017; Cangiano and Grillner, 2018; McClellan, 2018).

338 Another unexpected observation is that rhythmogenesis in V2a-D neurons during slow, carangiform mode
339 relies on recurrent inhibition. Previous lesion and ablation studies in adult lampreys (Buchanan and
340 McPherson, 1995) and embryonic frogs (Moult et al., 2013) suggest reciprocal inhibition is essential for
341 rhythmogenesis, consistent with the half-center model. Our recordings from fast V2a-Ds are also consistent
342 with the importance of reciprocal inhibition in rhythmogenesis, however this is only during anguilliform
343 mode. Critically, lampreys and frog embryos use anguilliform swimming at all speeds (Hoff and Wassersug,
344 2000; McClellan et al., 2016), suggesting that this mode of swimming is more reliant on bilateral
345 coordination to sustain spinal rhythms.

346 On the other hand, the speed-dependent dominance of reciprocal versus recurrent inhibition is flipped
347 when considering pattern-forming V2a-B neurons. Until now recurrent inhibition was linked to limiting
348 motor output (Hultborn et al., 1979), not to rhythmogenesis (see, however, Linden and Berg, 2021). The
349 stronger recurrent inhibition we see in fast V2a-Bs during anguilliform swimming is consistent with this
350 role. As swimming speed increases, motor bursts must occupy a consistent fraction of the swim cycle to
351 ensure propulsive thrust and avoid co-incident bilateral activity (Grillner, 1974). Fast V2a-Bs have relatively
352 strong connections to fast motor neurons (Menelaou and McLean, 2019), so limiting their firing would
353 ensure that as swim frequency increases and cycle periods decrease, motor bursts decrease.

354 Among slow V2a-Bs recurrent inhibition is largely absent in favor of reciprocal inhibition. Assuming they
355 follow the same connectivity rules as fast V2a-B types, this means at lower frequencies there is a greater
356 capacity for longer motor bursts via a broader window of premotor excitation. This supports our recent
357 study exploring the contribution of V2a-D and V2a-B neurons to slow biased swimming during optomotor
358 responses (Jay et al., 2023). Optomotor responses in larval zebrafish involve increases in the duration of
359 motor output on one side via unilateral recruitment of motor neurons, without impacting the timing of left-
360 right or head-tail coordination. While V2a-D neurons are agnostic to turn direction, V2a-Bs are selectively
361 recruited on the turning side. This provides a mechanism to decouple swim intensity and frequency, as
362 required for direction control during locomotion.

363 In adult zebrafish, V2a and motor neurons have been grouped into slow, intermediate, fast and escape
364 modules based on patterns of recruitment and phasic synaptic drive during fictive swimming (El Manira,
365 2023). In larvae, we also observe recruitment patterns among V2a neurons that would qualify as slow,
366 intermediate, fast and escape (c.f., Fig. 2G). However, we also find that recruitment probability varies based
367 on morphological type, with V2a-D neurons always firing more sparsely than V2a-B neurons, regardless of
368 speed. Collectively, these observations suggest that increases in speed in adults and larvae are initially
369 accomplished via more reliable V2a neuron recruitment, as reported in mice (Zhong et al., 2011). This fits
370 studies of motor neurons, where relatively low initial forces rely on recruitment (Enoka and Duchateau,
371 2017; Jay et al., 2023), while higher forces are achieved by increasing firing rates (Bhatt et al., 2007; Enoka
372 and Duchateau, 2017), in addition to silencing more easily recruited neurons (Smith et al., 1980; Kyriakatos
373 et al., 2011; Menelaou and McLean, 2012).

374 In sum, our findings suggest that cell-type-specific modes of spinal rhythmogenesis are responsible for
375 different speeds of locomotion. Studies in mice have implicated En1-labeled V1 interneurons not only in
376 reciprocal inhibition (Zhang et al., 2014), but also in recurrent inhibition, perhaps most famously via
377 Renshaw cells (Alvarez et al., 2005). The hierarchical and modular nature of recurrent inhibition we find
378 here could explain the relative challenge disentangling the role of V1 neurons in rhythm-generation versus
379 pattern-formation in both zebrafish (Kimura and Higashijima, 2019) and mice (Gosgnach et al., 2006).
380 Ultimately, these observations suggest that a common mechanism of rhythmogenesis is insufficient to
381 explain the full range operational range of locomotion.

382 **Materials and methods**

383 **Fish husbandry**

384 Tg[Chx10:GFP] fish (ZFIN ID: ZDB-ALT-061204-2) were used to target V2a neurons in the spinal cord
385 (Kimura et al., 2006). Fish were maintained at 28.5°C on a 14 hr light/10 hr dark cycle in an aquatics facility
386 staffed by Northwestern University's Center for Comparative Medicine. All experiments were performed at
387 room temperature between 4 and 5 days post fertilization (dpf) when zebrafish larvae are free swimming.
388 Because 4-5 dpf larvae have not yet developed secondary sexual characteristics, their sex cannot be easily
389 determined. Therefore, experiments were performed on larvae of either sex. All experimental protocols

390 conform to National Institutes of Health guidelines on animal experimentation and were approved by the
391 Northwestern University Institutional Animal Care and Use Committee (IS00019359 and IS00019319).

392 **Electrophysiology**

393 Electrophysiological recordings were acquired using a Multiclamp 700A amplifier (Molecular Devices), a
394 Digidata series 1322A digitizer (Molecular Devices), and pClamp 10 software (Molecular Devices). The
395 intrinsic firing patterns of V2a neurons were assessed by performing 500 ms long current steps at 1-2x
396 rheobase in current-clamp mode. To compare the intrinsic firing properties of V2a neurons to their
397 recruitment profiles during 'fictive' escape swimming, we performed simultaneous whole cell current-
398 clamp recordings of V2a neurons and extracellular recordings of the peripheral ventral rootlet. Synaptic
399 currents during fictive swimming were assessed in dual whole voltage-clamp and extracellular rootlet
400 recordings. Swimming was evoked by applying a mild and brief electrical shock (2-10 V; 0.1-0.4 ms) using
401 a bipolar tungsten electrode placed over the tail fin.

402 For recordings larvae were first paralyzed using alpha-bungarotoxin (1 mg/mL in extracellular solution
403 containing 134 mM NaCl, 2.9 mM KCl, 1.2 mM $MgCl_2$, 10 mM HEPES, 10 mM glucose, and 2.1 mM $CaCl_2$,
404 adjusted to pH 7.8 with NaOH), immersed in extracellular solution containing anesthetic (MS-222), and
405 secured left side up on a sylgard lined glass bottom dish using custom etched tungsten pins through the
406 notochord. To record the activity of the peripheral ventral rootlets, the skin over the muscle tissue at the
407 midbody was removed using fine forceps. For access to spinal V2a neurons, the muscle tissue over one
408 spinal segment was dissected away using a tool fashioned from sharpened tungsten wire. After the
409 dissection, the preparation was rinsed and immersed in anesthetic-free extracellular solution. For cell-
410 attached and whole cell recordings, standard-wall (1 mm outer diameter) borosilicate capillaries (Sutter
411 Instrument) were pulled to resistances between 5–16 MΩ using a micropipette puller (Flaming/Brown;
412 Sutter Instrument). For peripheral motor nerve recordings, electrodes were made by pulling a patch
413 electrode, breaking the tip, and then heat polishing and bending it using a microforge (MF-830; Narishige)
414 to offset the approach angle for better contact between the electrode and muscle tissue. Peripheral motor
415 nerve recordings were made no more than two segments caudal to the site of cellular recording.

416 For current clamp recordings, patch electrodes were filled with intracellular solution containing (125–130
417 mM K-gluconate, 2–4 mM MgCl2, 0.2–10 mM EGTA, 10 mM HEPES, 4 mM Na2ATP, adjusted to pH 7.3
418 with KOH). For voltage clamp recordings, the intracellular solution consisted of 122 mM $CsMeSO_3$, 0.1–1
419 mM QX314-Cl, 1 mM TEA-Cl, 3 mM $MgCl_2$, 10 mM HEPES, 1 mM EGTA, and 4 mM Na_2-ATP. $CsMeSO_3$ and
420 QX-314 Cl were included in the solution to block voltage dependent channels. Alexa Fluor 568 hydrazide
421 (50 μmol/l) was also added to the intracellular solution for the post-hoc confirmation of cell identity.

422 V2a neurons were targeted on an epifluorescent microscope (Axio Examiner) under a 40×/1.0 NA water-
423 immersion objective (W Plan-Apochromat; Zeiss) using a CCD camera (Rolera-XR; QImaging). The
424 electrode was positioned using a motorized micromanipulator (MP-225; Sutter Instrument or Patchstar,

425 Scientifica), while positive pressure was maintained using a pneumatic transducer (Model DPM-1B; Bio-
426 Tek Instruments) to prevent the tip from clogging as the neuron was approached. The neuron was held at -
427 65 mV during GΩ seal formation. Once the seal was achieved, for voltage-clamp experiments cell attached
428 recordings were performed to obtain the recruitment patterns of V2a neurons during fictive escape
429 swimming before breaking into the neuron to record synaptic currents. A 5 mV hyperpolarizing pulse was
430 then administered at a holding potential of -65 mV, and the steady state current injected during the pulse
431 was used to compute input resistance according to Ohm's law.

432 Excitatory currents were clamped at the reversal potential for inhibition calculated from our solutions,
433 which is -75 mV and inhibitory currents were clamped at the reversal potential for excitation, which is + 10
434 mV. These values were corrected for a calculated junction potential of –11 mV. Thus, neurons were
435 alternately held at the corrected potentials of -64 mV for EPSCs and 21 mV for IPSCs. To monitor series
436 resistance throughout the experiment, recordings were alternately performed without and with 60% series
437 resistance compensation. Standard corrections for bridge balance and electrode capacitance were applied
438 for current clamp recordings. Whole-cell electrical signals were filtered at 10 kHz and digitized at 100 kHz
439 at a gain of 10 (feedback resistor, 500 MΩ). Extracellular signals from the peripheral motor nerves were
440 amplified at a gain of 1000 and digitized with low-frequency and high-frequency cutoffs set at 300 and
441 5000 Hz, respectively.

442 **Imaging**

443 After each electrophysiological recording, a series of epifluorescent and differential interference contrast
444 images were captured using a CCD camera (Rolera-XR) and QCapture Suite imaging software (QImaging)
445 to track the axonal trajectories of V2a neurons and confirm their morphology. Images were later analyzed
446 in ImageJ.

447 **Data analysis**

448 Soma size and dorsoventral locations of individually labeled V2a neurons were measured in ImageJ.
449 Dorsoventral (DV) and mediolateral (ML) positions of V2a neurons in Tg[Chx10:GFP] were computed by
450 obtaining the relevant positional coordinates from confocal images in Imaris (Oxford Instruments). Briefly,
451 the spot detection tool was used to obtain the coordinates of the centers of all somata and orthogonal slicers
452 were used in conjunction with measurement points to extract the coordinates of the dorsoventral and lateral
453 boundaries of the spinal cord as well as the central canal. The positions of the somata were then respectively
454 normalized against the positions of the dorsoventral and mediolateral boundaries to get the final DV and
455 ML positions. V2a somata were classified into two groups based on the intensity of GFP expression. The
456 GFP fluorescence intensity of V2a somata was exported from Imaris, and its density distribution was plotted
457 in R. Because the density distribution of GFP fluorescence intensity was bimodal, the minimum between
458 the two modes of the distribution was used as a cut off to split V2a neurons into classes of low and high GFP
459 expression.

Whole cell and extracellular recordings were annotated in Dataview to label individual spikes, ventral rootlet bursts and swimming episodes. The onset and duration of spikes, ventral root bursts and swimming episodes were then batch exported into text files, which were then read into MATLAB (Mathworks) for further analysis. Instantaneous spike frequencies are the inverse of the period between two successive action potentials. The recruitment patterns of V2a neurons were quantified by computing the probability of observing spikes for all cycles present within each 5 Hz ventral root burst frequency bin from 10 Hz to 65 Hz. The recruitment probability was then plotted as a function of ventral root burst frequency. The V2a neurons with an upward sloping recruitment reliability plot were classified as fast and those with a downward sloping plot were categorized as slow (cf. trendlines in Fig. 4E)

Maximum excitatory and inhibitory currents reflect the maximum current received at any ventral root burst frequency. To compare frequency dependent changes in synaptic currents across neuron types, they were normalized against the maximum synaptic current the neuron received. Normalized currents were then averaged in four discrete frequency bins spanning carangiform and anguilliform swimming modes (15-25, 25-35, 35-45, 45+ Hz). To analyze the phasic timing of spiking and synaptic currents, they were normalized to the period of the corresponding cycle, such that the centers of successive motor bursts marked phase 0 and phase 1. Synaptic currents arriving between 0.75 to 0.25 , were considered in-phase and those between 0.25 and 0.75 considered anti-phase. To analyze the relative timing of excitation and inhibition (Fig. 6A, D and E), we normalized amplitudes to the maximum current received in each cycle, such that the final values of normalized current ranged between 0 and 1. Currents were then averaged for all cycles present within the four frequency bins

To quantify peaks in synaptic currents corresponding to the phasic inputs received during a swim cycle, current traces were low pass filtered at the cutoff frequency of 1000 Hz using the butterworth (second order) and zero phase digital filters in MATLAB. The latter was used to prevent the raw current values from undergoing a phase shift. Peaks were detected using the findpeaks() function in MATLAB. Counts of V2a spikes, EPSC's and IPSC's were plotted on a circular axis from phase 0 to 1. Data visualization and statistical analysis were performed in R.

Statistics

All data were first tested for normality to select the appropriate statistical test. None of the data were normally distributed, so nonparametric tests were used to assess statistical significance. The difference between the density distributions of mediolateral and dorsoventral somatic positions was tested using the Two-sample Kolmogorov-Smirnov test. Correlation between peak synaptic current and input resistance was tested using Spearman's rank correlation test. Comparisons between two groups of paired or unpaired data were performed using the Wilcoxon signed-rank test and the Wilcoxon rank sum test, respectively. For circular plots, Watson's two-sample test of homogeneity was used to determine whether the spike and post synaptic current distributions in two conditions were significantly different from each other. Statistically significant differences are denoted as follows: $^{*}p < 0.05$; $^{**}p < 0.01$; $^{***}p < 0.001$. Note that it was not

always possible to collect cell-attached data and voltage-clamp recordings of excitation and inhibition in the same cells, so n numbers reported in the text can vary between conditions.

References

Alvarez FJ, Jonas PC, Sapir T, Hartley R, Berrocal MC, Geiman EJ, Todd AJ, Goulding M (2005) Postnatal phenotype and localization of spinal cord V1 derived interneurons. J Comp Neurol 493:177-192.

Ausborn J, Shevtsova NA, Caggiano V, Danner SM, Rybak IA (2019) Computational modeling of brainstem circuits controlling locomotor frequency and gait. Elife 8:e43587.

Bello-Rojas S, Istrate AE, Kishore S, McLean DL (2019) Central and peripheral innervation patterns of defined axial motor units in larval zebrafish. J Comp Neurol 527:2557-2572.

Bhatt DH, McLean DL, Hale ME, Fetcho JR (2007) Grading movement strength by changes in firing intensity versus recruitment of spinal interneurons. Neuron 53:91-102.

Bhattacharyya K, McLean DL, MacIver MA (2021) Intersection of motor volumes predicts the outcome of ambush predation of larval zebrafish. J Exp Biol 224:jeb235481.

Brocard F, Tazerart S, Vinay L (2010) Do pacemakers drive the central pattern generator for locomotion in mammals? Neuroscientist 16:139-155.

Brown TG (1911) The intrinsic factors in the act of progression in the mammal. Proc R Soc B – Biol Sci 84:308-319.

Buchanan JT (2018) Swimming rhythm generation in the caudal hindbrain of the lamprey. J Neurophysiol 119:1681-1692.

Buchanan JT, McPherson DR (1995) The neuronal network for locomotion in the lamprey spinal cord: evidence for the involvement of commissural interneurons. J Physiol Paris 89:221-233.

Budick SA, O'Malley DM (2000) Locomotor repertoire of the larval zebrafish: swimming, turning and prey capture. J Exp Biol 203:2565-2579.

Cangiano L, Grillner S (2018) Commentary: elimination of left-right reciprocal coupling in the adult lamprey spinal cord abolishes the generation of locomotor activity. Front Neural Circuits 12:34.

D'Elia KP, Hameedy H, Goldblatt D, Frazel P, Kriese M, Zhu Y, Hamling KR, Kawakami K, Liddelow SA, Schoppik D, Dasen JS (2023) Determinants of motor neuron functional subtypes important for locomotor speed. Cell Rep 42:113049.

Di Santo V, Goerig E, Wainwright DK, Akanyeti O, Liao JC, Castro-Santos T, Lauder GV (2021) Convergence of undulatory swimming kinematics across a diversity of fishes. Proc Natl Acad Sci U S A 118:e2113206118.

Dougherty KJ, Kiehn O (2010) Firing and cellular properties of V2a interneurons in the rodent spinal cord. J Neurosci 30:24-37.

El Manira A (2023) Modular circuit organization for speed control of locomotor movements. Curr Opin Neurobiol 82:102760.

532 Enoka RM, Duchateau J (2017) Rate coding and the control of muscle force. Cold Spring Harb Perspect
533 Med 7.
534 Feldman JL (1986) Neurophysiology of breathing in mammals. In: Handbook of Physiology, The Nervous
535 System, Intrinsic Regulatory Systems (Terjung R, ed).
536 Gosgnach S, Lanuza GM, Butt SJ, Saueressig H, Zhang Y, Velasquez T, Riethmacher D, Callaway EM,
537 Kiehn O, Goulding M (2006) V1 spinal neurons regulate the speed of vertebrate locomotor
538 outputs. Nature 440:215-219.
539 Grillner S (1974) On the generation of locomotion in the spinal dogfish. Exp Brain Res 20:459-470.
540 Grillner S (1981) Control of locomotion in bipeds, tetrapods, and fish. In: Handbook of Physiology, The
541 Nervous System, Motor Control (Terjung R, ed).
542 Grillner S (1985) Neurobiological bases of rhythmic motor acts in vertebrates. Science 228:143-149.
543 Grillner S, Kozlov A (2021) The CPGs for limbed locomotion-facts and fiction. Int J Mol Sci 22:5882.
544 Guertin PA (2009) The mammalian central pattern generator for locomotion. Brain Res Rev 62:45-56.
545 Hayashi M, Hinckley CA, Driscoll SP, Moore NJ, Levine AJ, Hilde KL, Sharma K, Pfaff SL (2018) Graded
546 arrays of spinal and supraspinal V2a interneuron subtypes underlie forelimb and hindlimb motor
547 control. Neuron 97:869-884 e865.
548 Hoff KV, Wassersug RJ (2000) Tadpole locomotion: axial movement and tail functions in a largely
549 vertebraeless vertebrate. American Zoologist 40:62-76.
550 Hultborn H, Lindstrom S, Wigstrom H (1979) On the function of recurrent inhibition in the spinal cord.
551 Exp Brain Res 37:399-403.
552 Jay M, MacIver MA, McLean DL (2023) Spinal basis of direction control during locomotion in larval
553 zebrafish. J Neurosci 43:4062-4074.
554 Kimura Y, Higashijima SI (2019) Regulation of locomotor speed and selection of active sets of neurons by
555 V1 neurons. Nat Commun 10:2268.
556 Kimura Y, Okamura Y, Higashijima S (2006) alx, a zebrafish homolog of Chx10, marks ipsilateral
557 descending excitatory interneurons that participate in the regulation of spinal locomotor circuits.
558 J Neurosci 26:5684-5697.
559 Kimura Y, Satou C, Fujioka S, Shoji W, Umeda K, Ishizuka T, Yawo H, Higashijima S (2013) Hindbrain
560 V2a neurons in the excitation of spinal locomotor circuits during zebrafish swimming. Curr Biol
561 23:843-849.
562 Kishore S, Bagnall MW, McLean DL (2014) Systematic shifts in the balance of excitation and inhibition
563 coordinate the activity of axial motor pools at different speeds of locomotion. J Neurosci
564 34:14046-14054.
565 Kozlov A, Huss M, Lansner A, Kotaleski JH, Grillner S (2009) Simple cellular and network control
566 principles govern complex patterns of motor behavior. Proc Natl Acad Sci U S A 106:20027-
567 20032.
568 Kyriakatos A, Mahmood R, Ausborn J, Porres CP, Buschges A, El Manira A (2011) Initiation of locomotion
569 in adult zebrafish. J Neurosci 31:8422-8431.

570 Li WC, Roberts A, Soffe SR (2010) Specific brainstem neurons switch each other into pacemaker mode to
571 drive movement by activating NMDA receptors. J Neurosci 30:16609-16620.
572 Linden H, Berg RW (2021) Why firing rate distributions are important for understanding spinal central
573 pattern generators. Front Hum Neurosci 15:719388.
574 Marder E, Calabrese RL (1996) Principles of rhythmic motor pattern generation. Physiol Rev 76:687-717.
575 Marder E, Bucher D (2001) Central pattern generators and the control of rhythmic movements. Curr Biol
576 11:R986-996.
577 McClellan AD (2018) Response: commentary: elimination of left-right reciprocal coupling in the adult
578 lamprey spinal cord abolishes the generation of locomotor activity. Front Neural Circuits 12:62.
579 McClellan AD, Pale T, Messina JA, Buso S, Shebib A (2016) Similarities and differences for swimming in
580 larval and adult lampreys. Physiol Biochem Zool 89:294-312.
581 McCrea DA, Rybak IA (2008) Organization of mammalian locomotor rhythm and pattern generation.
582 Brain Res Rev 57:134-146.
583 McHenry MJ, Lauder GV (2006) Ontogeny of form and function: locomotor morphology and drag in
584 zebrafish (Danio rerio). J Morphol 267:1099-1109.
585 McLean DL, Fetcho JR (2009) Spinal interneurons differentiate sequentially from those driving the
586 fastest swimming movements in larval zebrafish to those driving the slowest ones. J Neurosci
587 29:13566-13577.
588 McLean DL, Dougherty KJ (2015) Peeling back the layers of locomotor control in the spinal cord. Curr
589 Opin Neurobiol 33:63-70.
590 McLean DL, Fan J, Higashijima S, Hale ME, Fetcho JR (2007) A topographic map of recruitment in
591 spinal cord. Nature 446:71-75.
592 McLean DL, Masino MA, Koh IY, Lindquist WB, Fetcho JR (2008) Continuous shifts in the active set of
593 spinal interneurons during changes in locomotor speed. Nat Neurosci 11:1419-1429.
594 Menelaou E, McLean DL (2012) A gradient in endogenous rhythmicity and oscillatory drive matches
595 recruitment order in an axial motor pool. J Neurosci 32:10925-10939.
596 Menelaou E, McLean DL (2019) Hierarchical control of locomotion by distinct types of spinal V2a
597 interneurons in zebrafish. Nat Commun 10:4197.
598 Menelaou E, VanDunk C, McLean DL (2014) Differences in the morphology of spinal V2a neurons reflect
599 their recruitment order during swimming in larval zebrafish. J Comp Neurol 522:1232-1248.
600 Menelaou E, Kishore S, McLean DL (2022) Mixed synapses reconcile violations of the size principle in
601 zebrafish spinal cord. Elife 11.
602 Messina JA, St Paul A, Hargis S, Thompson WE, McClellan AD (2017) Elimination of left-right reciprocal
603 coupling in the adult lamprey spinal cord abolishes the generation of locomotor activity. Front
604 Neural Circuits 11:89.
605 Moult PR, Cottrell GA, Li WC (2013) Fast silencing reveals a lost role for reciprocal inhibition in
606 locomotion. Neuron 77:129-140.

607 Muller UK, van Leeuwen JL (2004) Swimming of larval zebrafish: ontogeny of body waves and
608 implications for locomotory development. J Exp Biol 207:853-868.
609 Myers P, Eisen J, Westerfield M (1986) Development and axonal outgrowth of identified motorneurons in
610 the zebrafish. J Neurosci 6:2278-2289.
611 Parker D (2017) The lesioned spinal cord is a “new" spinal cord: evidence from functional changes after
612 spinal injury in lamprey. Front Neural Circuits 11:84.
613 Patterson BW, Abraham AO, MacIver MA, McLean DL (2013) Visually guided gradation of prey capture
614 movements in larval zebrafish. J Exp Biol 216:3071-3083.
615 Picton LD, Bjornfors ER, Fontanel P, Pallucchi I, Bertuzzi M, El Manira A (2022) Developmental switch
616 in the function of inhibitory commissural V0d interneurons in zebrafish. Curr Biol 32:3515-3528.
617 Ryczko D, Dubuc R, Cabelguen JM (2010) Rhythmogenesis in axial locomotor networks: an interspecies
618 comparison. Prog Brain Res 187:189-211.
619 Satou C, Sugioka T, Uemura Y, Shimazaki T, Zmarz P, Kimura Y, Higashijima SI (2020) Functional
620 diversity of glycinergic commissural inhibitory neurons in larval zebrafish. Cell Rep 30:3036-
621 3050.
622 Smith JL, Betts B, Edgerton VR, Zernicke RF (1980) Rapid ankle extension during paw shakes: selective
623 recruitment of fast ankle extensors. J Neurophysiol 43:612-620.
624 Song J, Pallucchi I, Ausborn J, Ampatzis K, Bertuzzi M, Fontanel P, Picton LD, El Manira A (2020)
625 Multiple rhythm-generating circuits act in tandem with pacemaker properties to control the start
626 and speed of locomotion. Neuron 105:1048-1061.
627 Soto AP, McHenry MJ (2020) Pursuit predation with intermittent locomotion in zebrafish. J Exp Biol
628 223:jeb230623.
629 Talpalar AE, Bouvier J, Borgius L, Fortin G, Pierani A, Kiehn O (2013) Dual-mode operation of neuronal
630 networks involved in left-right alternation. Nature 500:85-88.
631 Thorsen DH, Cassidy JJ, Hale ME (2004) Swimming of larval zebrafish: fin-axis coordination and
632 implications for function and neural control. J Exp Biol 207:4175-4183.
633 Wiggin TD, Anderson TM, Eian J, Peck JH, Masino MA (2012) Episodic swimming in the larval zebrafish
634 is generated by a spatially distributed spinal network with modular functional organization. J
635 Neurophysiol 108:925-934.
636 Zhang J, Lanuza GM, Britz O, Wang Z, Siembab VC, Zhang Y, Velasquez T, Alvarez FJ, Frank E, Goulding
637 M (2014) V1 and V2b interneurons secure the alternating flexor-extensor motor activity mice
638 require for limbed locomotion. Neuron 82:138-150.
639 Zhong G, Sharma K, Harris-Warrick RM (2011) Frequency-dependent recruitment of V2a interneurons
640 during fictive locomotion in the mouse spinal cord. Nat Commun 2:274.
641 Zhong G, Droho S, Crone SA, Dietz S, Kwan AC, Webb WW, Sharma K, Harris-Warrick RM (2010)
642 Electrophysiological characterization of V2a interneurons and their locomotor-related activity in
643 the neonatal mouse spinal cord. J Neurosci 30:170-182.

644 Ziskind-Conhaim L, Hochman S (2017) Diversity of molecularly defined spinal interneurons engaged in
645 mammalian locomotor pattern generation. J Neurophysiol 118:2956-2974.

646

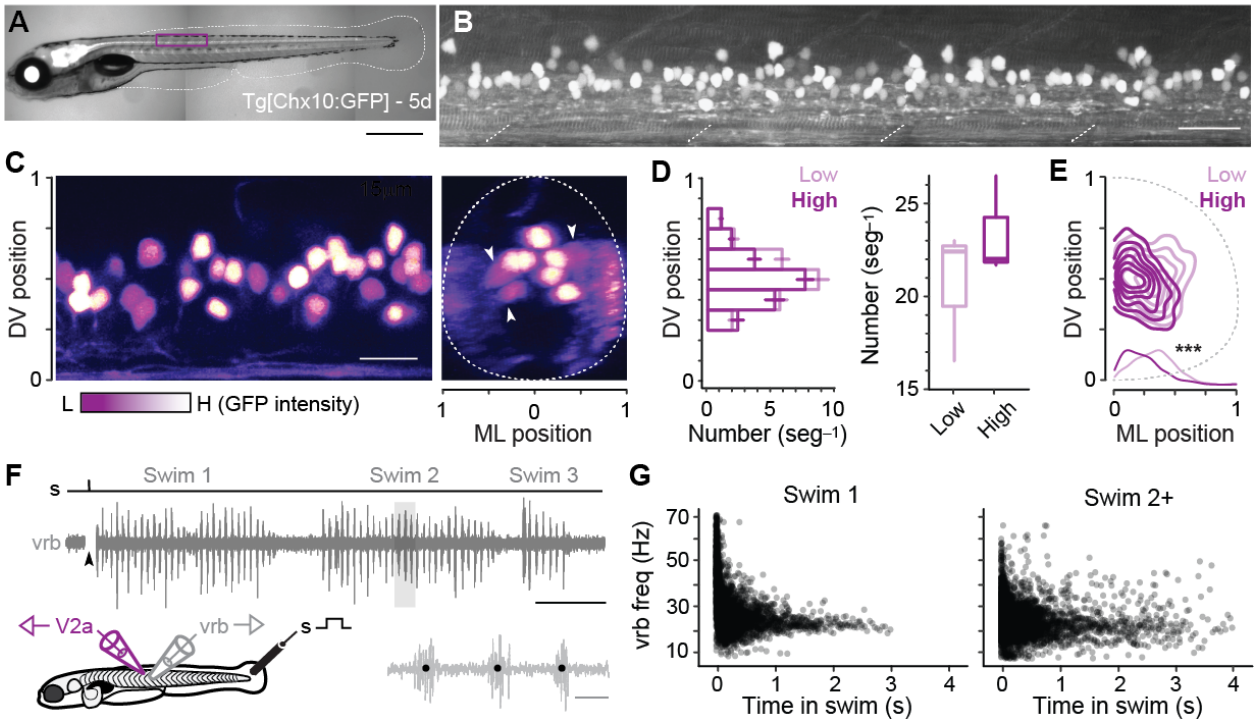

Figure 1: Identification of V2a neurons for recordings during 'fictive' swimming

A) Composite DIC/epifluorescence image of Tg[Chx10:GFP] larval zebrafish at 5 days post fertilization (5d). Scale bar, 0.5 mm.

B) Confocal image of the Tg[Chx10:GFP] spinal cord from segments 10-15 at midbody (purple box in *A*). Scale bar, 30 μm.

C) Pseudo-colored images of V2a somata based on high (H, white) and low (L, purple) GFP intensity. Left panel: sagittal section, right panel: coronal section. Dashed lines indicate boundaries of spinal cord, which are normalized to 0-1 in the dorso-ventral and medio-lateral axes. White arrowheads indicate large, lateral V2a somata with low levels of GFP expression. Scale bar, 20 μm.

D) Plots of numbers of low and high intensity V2a neurons per midbody segment (n = 5-6 segments from 3 fish). Left panel: Bar plot of average number (+/- SEM) of low and high GFP V2a neurons along the dorsoventral (DV) axis. There is no significant difference in the medians of the dorsoventral distributions of high and low GFP expressing V2a neurons (Wilcoxon rank-sum rest; W = 68479, p = 0.6975, n = 347 high and 401 low GFP neurons from 3 fish). Right panel: Box and whisker plot showing average number of high and low GFP neurons per segment (Wilcoxon rank-sum test, W = 88, p = 0.05269, n = 17 segments in 3 fish).

E) Two-dimensional contour density plots showing the mediolateral (ML) and dorsoventral (DV) distributions of V2a neurons expressing low or high levels of GFP. Density distributions of ML positions of V2a neurons are shown at the bottom of the contour plots, which are significantly different (***, Two-

sample Kolmogorov-Smirnov test, D = 0.16452, p = 8.46×10^{-05}, n = 347 high and 401 low GFP neurons from 3 fish).

F) Top panel: an example of an extracellular ventral rootlet recording of three consecutive swim episodes evoked by a mild electrical stimulus (s) to the tail fin (at arrowhead, artifact blanked). Scale bar, 500 ms. Bottom left panel: a cartoon of the locations of the stimulus and the recording electrodes. Bottom right panel: individual ventral rootlet bursts (vrb) on an expanded timescale. Black dots mark the center of each vrb used to calculate swim frequency in Hz (1/s), which is indicative of swimming speed. Scale bar, 20 ms.

G) Scatter plot of vrb frequency (Hz) versus the time in swim episode (ms). The swimming episode immediately following the stimulus is called Swim 1 (left), and any subsequent swimming episodies are called Swim 2+ (right).

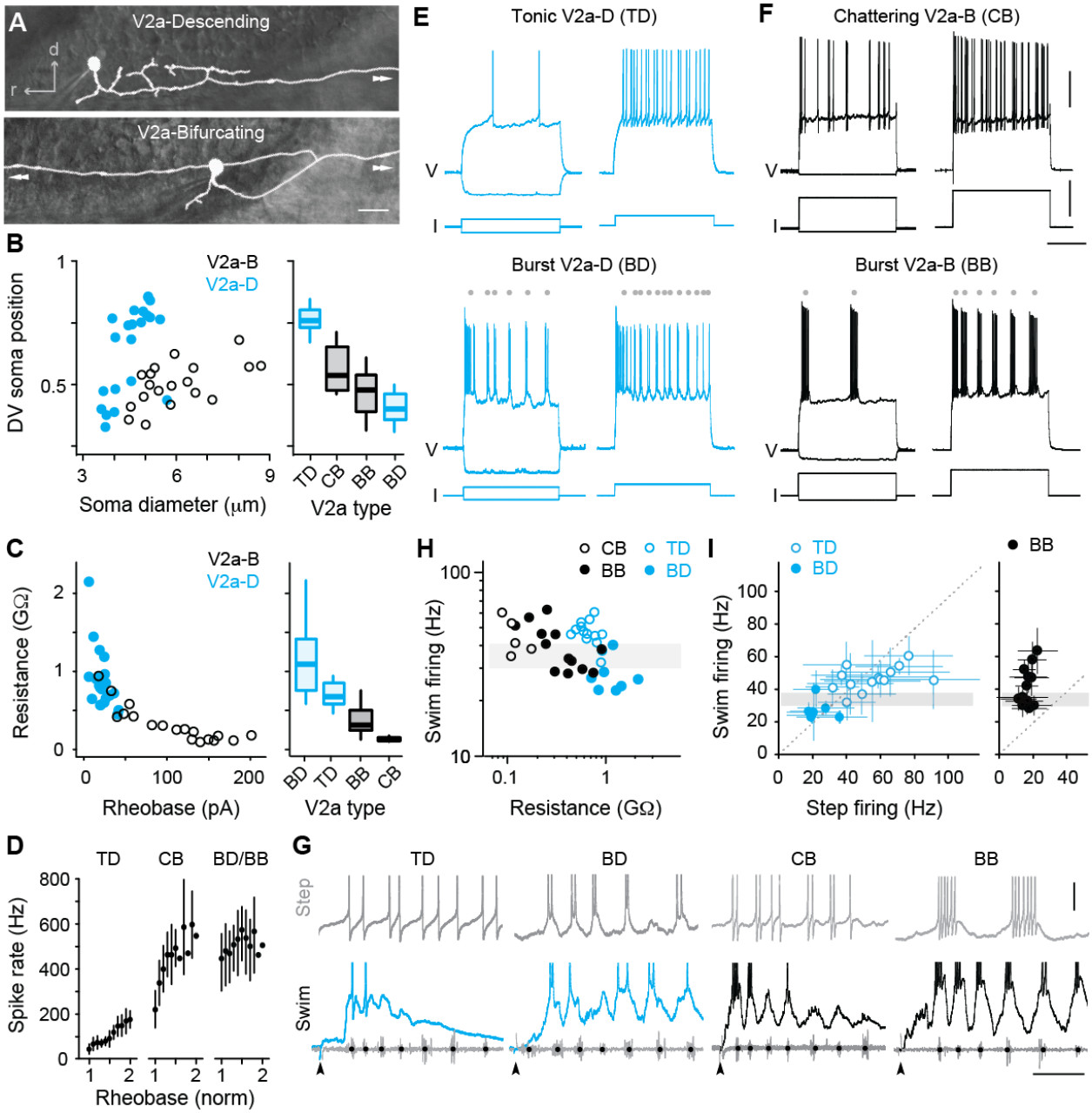

Figure 2: Cell-type-specific electrophysiological properties linked to recruitment order

A) Composite DIC/epifluorescent images of post-hoc fills of V2a-Descending (V2a-D, top) and V2a-Bifurcating (V2a-B, bottom) neurons. Arrows indicate continuation of axons outside the field of view. Scale bar, 10 μm.

B) Left panel: scatter plot of soma positions of V2a-D and V2a-B neurons normalized to dorsoventral (DV) position, with 1 demarcating the dorsal and 0 the ventral boundaries of the spinal cord. Right panel: boxplots of dorso-ventral soma positions of V2a-D and V2a-B neurons classified as tonic, bursting, or chattering based on their step-firing responses in panels *E* and *F*. TD= tonic V2a-D, CB=chattering V2a-B, BB=bursting V2a-B, BD=bursting V2a-D.

C) Left panel: scatter plot of input resistance (GΩ) versus the rheobase (pA) of V2a-B (black) and V2a-D (blue) neurons. Right panel: Box plots of input resistance (GΩ) of BD, TD, BB, and CB V2a neurons.

D) Mean (+/– SD) instantaneous spike rates (Hz) between 1-2x rheobase for TD, CB, BD and BB neurons.

E) Top panel: step-firing responses of V2a-D neurons defined as tonic (TD). Bottom panel: step-firing responses of V2a-D neurons defined as bursting (BD). Grey dots depict the midpoint of slower membrane oscillations driving the bursting spiking behavior. Same scale as panel *F*.

F) Top panel: step-firing responses of V2a-B neurons defined as chattering (CB). Bottom panel: V2a-B neurons defined as bursting (BB). Grey dots depict the midpoint of slower membrane oscillations driving the bursting spiking behavior. Scale bars, 20 mV, 200 pA, 200 ms.

G) Top panels: Step-firing responses close to rheobase of TD, BD, CB, and BB neurons. Bottom panels: Swim firing responses evoked by a mild electrical shock shown on the same time scales. Black dots on ventral root bursts (grey) indicate swim frequency. Black arrows mark the stimulation artifact. Scale bars, 10 mV, 50 ms.

H) Scatter plot of median swim firing frequency (Hz) versus the input resistance (GΩ) of CB, TD, BB, and BD on logarithmic x- and y-scales. Shaded grey box indicates 30-40 Hz range reflecting transition between anguilliform and carangiform swim modes.

I) A comparison of median swim-firing and median step-firing frequencies between 1-2x rheobase (+/– SD) for TD, BD, and BB neurons. For TD neurons, step frequencies represent spike rates, while for BD and BB neurons they represent burst rates. CB neurons were too variable in step firing frequency to obtain reliable median values. Shaded grey box indicates 30-40 Hz range reflecting transition between anguilliform and carangiform swim modes.

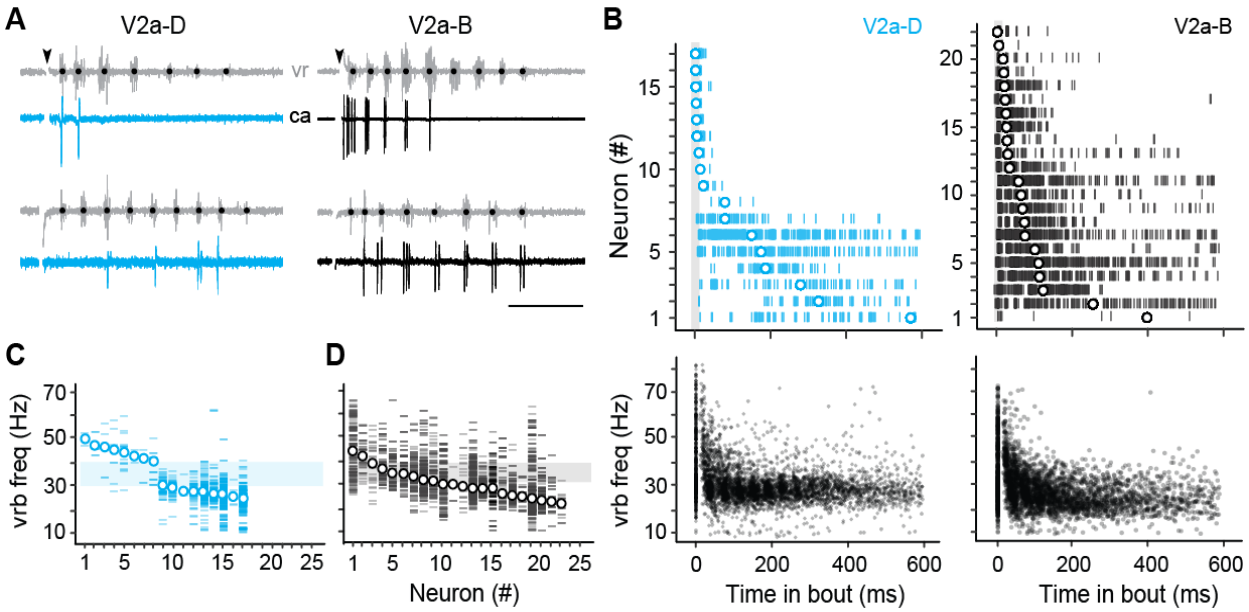

Figure 3: Differences in recruitment patterns among the distinct V2a types

A) Left panel: Cell-attached (ca) recordings of descending V2a (V2a-D) neurons during fictive swimming evoked by a brief stimulus (at black arrowhead). Black dots on ventral root (vr) bursts (grey) indicate swim frequency. The top neuron fires immediately after the stimulus during high frequency swimming, while the bottom neuron fires near the end of the episode at lower frequencies. Right panel: As shown to the left, but for bifurcating V2a (V2a-B) neurons. Scale bar, 100 ms.

B) Top panel: spike timing of V2a-D (left) and V2a-B (right) neurons relative to the start of swimming ordered by the median of the distribution. Bottom panel: A scatterplot of vrb frequency (Hz) as a function of time for all episodes (Swim 1 and 2+) during which the V2a-D (left) or V2a-B (right) neurons were recruited.

C) Raster plots of ventral root burst frequencies (Hz) over which V2a-Ds were recruited ordered by the median vrb recruitment frequency (Hz). Shaded box indicates 30-40 Hz range reflecting transition between anguilliform and carangiform swim modes.

D) Raster plots of ventral root burst frequencies (Hz) over which V2a-Bs were recruited ordered by the median vrb recruitment frequency (Hz). Shaded box indicates 30-40 Hz range reflecting transition between anguilliform and carangiform swim modes.

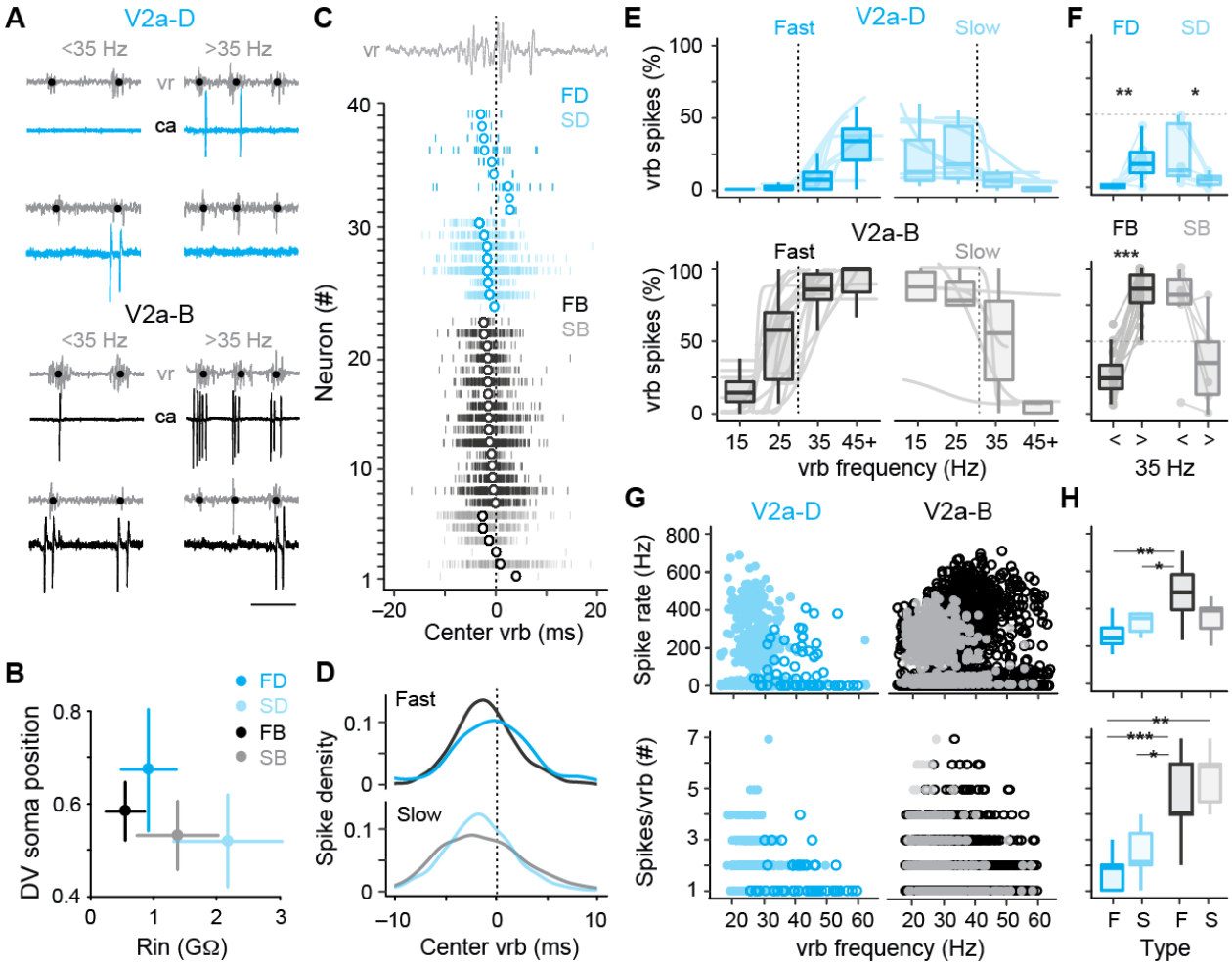

Figure 4: Distinct types of slow and fast V2a neurons distinguished based on recruitment

A) Top panel: Cell-attached (ca) and ventral rootlet (vr) recordings during slow (<35 Hz) and fast (>35 Hz) swimming illustrate V2a-D neurons (blue) that fire exclusively at slow and fast speeds. Bottom panel: V2a-B neurons (black) fire more reliably at both slow and fast speeds. Scale bar, 25 ms.

B) Plots of the mean (+/– SD) dorsoventral (DV) positions of fast (FD) and slow (SD) V2a-Ds, and fast (FB) and slow (SB) V2a-Bs versus their mean (+/– SD) input resistance (Rin).

C) Spike timing of slow (S) and fast (F) V2a-D and V2a-B neurons relative to the center of the ventral root burst (vrb) depicted by the dashed vertical line. Tick marks represent individual spikes from multiple cycles and circles represent median spike timing.

D) Density plots of spike timing relative to the center burst for slow and fast V2a-B and V2a-D neurons illustrated in panel *C*.

E) Top panel: Box plots of the percentage of ventral root bursts with spikes (vrb spikes %) as a function of vrb frequency (Hz) for fast (FD, n = 9) and slow (SD, n = 8) V2a-D neurons. For box plots, the ventral root burst frequency was binned at 15 Hz intervals starting at 15 Hz, and the final interval of 45+Hz consisted of a 20 Hz range spanning from 45-65 Hz. Box plots are superimposed on trendlines from

individual neurons fit to data binned at 5 Hz intervals, whose slopes define whether they are fast (positive) or slow (negative). Dashed line indicates transition between slow carangiform and fast anguilliform modes. Bottom panel: As above but for fast (FB, n = 16) and slow (SB, n = 6) V2a-B neurons.

F) Top panel: Box plots of vrb spikes % for slow and fast V2a-D neurons from panel E collapsed into single slow (<35 Hz) and (>35 Hz) bins for purposes of statistical analysis (Wilcoxon signed-rank test; FD, V = 1, p = 0.007812, n = 9; SD, V = 36, p = 0.007813, n = 8). Bottom panel: As above but for V2a-B neurons (Wilcoxon signed-rank test: FB, V = 0, p = 6.104e-05, n = 16; SB, V = 20, p = 0.0625, n = 6).

G) Top panel: Scatter plots of instantaneous spike rates versus vrb frequency (Hz) for V2a-D (left) and V2a-B (right) neurons color coded as fast (dark) and slow (light). FD, n = 9; SD, n = 8; FB, n = 16; SB; n = 6, Bottom panel: Scatter plots of the number of spikes per ventral root burst (#) as a function of vrb frequency (Hz), organized and color coded as above.

H) Top panel: Box plots of maximum instantaneous spike rates for fast (n = 5) and slow (n = 7) V2a-D and fast (n = 16) and slow (n = 5) V2a-B neurons. Note, only a subset of V2a neurons that fired two or more spikes per cycle were included in this analysis (Wilcoxon rank-sum test; FB-FD, W = 73, p = 0.00412,; FB-SD, W = 90, p = 0.02247). Bottom panel: Box plots of the maximum number of spikes/vrb (Wilcoxon rank-sum test; FB-FD, W = 132.5, p = 0.0005348,; FB-SD, W = 100.5, p = 0.024; FD-SB, W = 50, p = 0.00667; FD, n = 9; SD, n = 8; FB, n = 16; SB, n = 6).

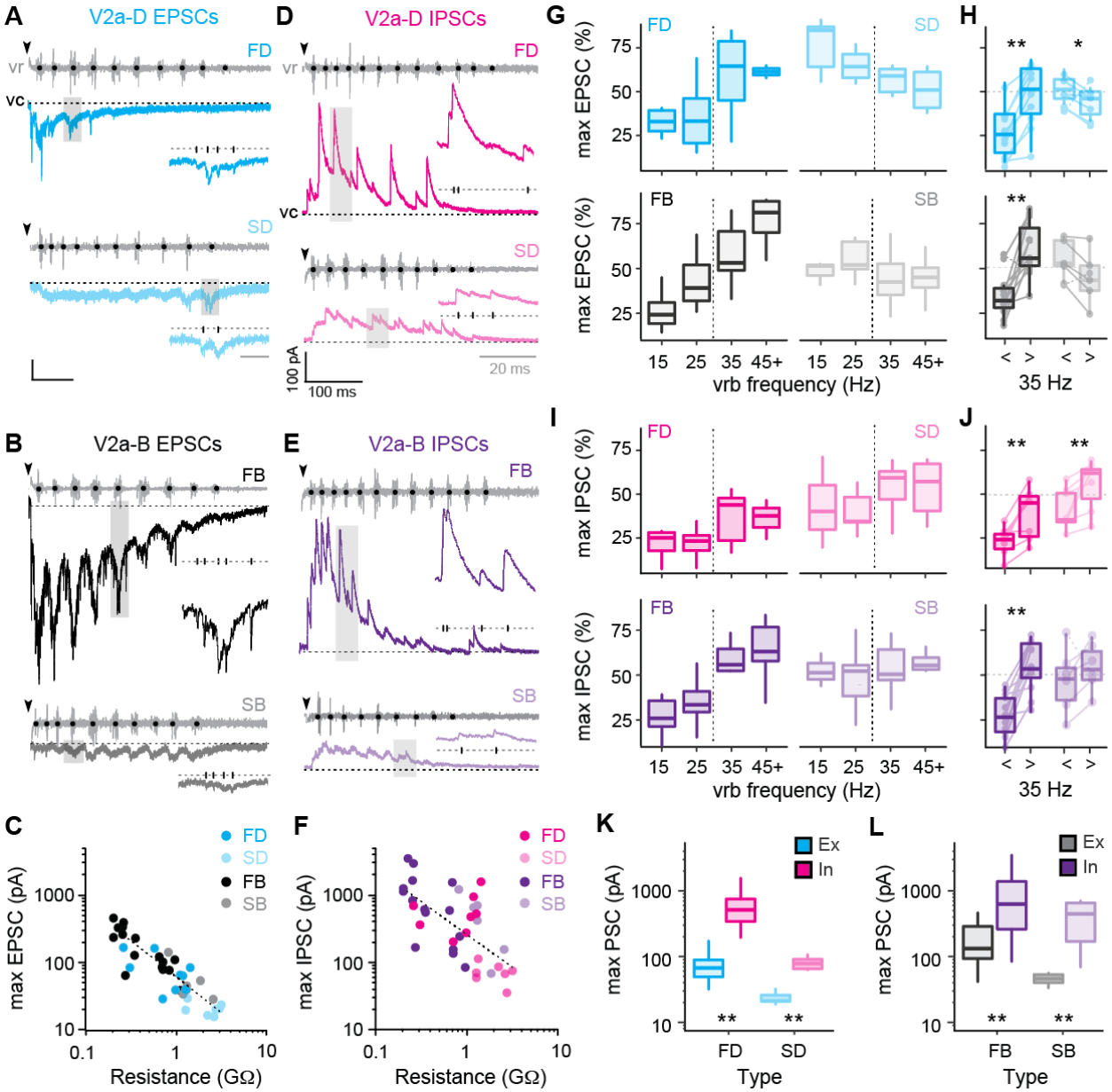

Figure 5: Differences in levels of synaptic drive related to speed and V2a cell type

A) Voltage-clamp (vc) recordings of excitatory post-synaptic currents (EPSCs) received by fast (top, FD) and slow (bottom, SD) V2a-D neurons along with ventral root (vr) recordings during fictive swimming triggered by an electrical stimulus (black arrowheads, artifact blanked). Black dots indicate burst intervals for frequency measures. Grey shaded boxes indicate region expanded inset, illustrating the holding potential (dashed line, -75 mV) and individual EPSCs (tick marks). Scale bars, 25 pA, 100 ms (20 ms inset).

B) As in *A*, but for fast (top, FB) and slow (bottom, SB) V2a-B neurons.

C) Scatter plot of maximum EPSC amplitude (pA) as a function of input resistance (GΩ) on logarithmic x- and y-scales. Dashed logarithmic trendlines are included for illustrative purposes (Spearman's rank correlation test, Rho = -0.8730769, $p < 2.2 \times 10^{-13}$, n = 39).

D) Voltage-clamp recordings of inhibitory post-synaptic currents (IPSCs) at a holding potential of 10 mV from fast (top, FD) and slow (bottom, SD) V2a-D neurons, organized as detailed in panel A. Scale bars, 100 pA, 100 ms (20 ms inset).

E) As in D, but fast (top, FB) and slow (bottom, SB) V2a-B neurons.

F) Scatter plot of maximum IPSC amplitude as a function of input resistance (GΩ) on logarithmic x- and y-scales (Spearman's rank correlation test; Rho = -0.6332046, $p = 5.041 \times 10^{-05}$, n = 36).

G) Top panel: Box plots of the maximum EPSC per cycle as a percentage of the maximum current (max EPSC%) for fast (FD, n = 9) and slow (SD, n = 6) V2a-D neurons, organized into 4 bins based on frequency. Dashed line indicates transition between slow carangiform and fast anguilliform modes. Bottom panel: as above, but for fast (FB, n = 11) and slow (SB, n = 5) V2a-B neurons.

H) Top panel: Box plots of max EPSC% for fast and slow V2a-D neurons from panel G, collapsed into single slow (<35 Hz) and fast (>35 Hz) bins for purposes of statistical analysis (Wilcoxon signed-rank test; FD, V = 0, p = 0.003906, n = 9; SD, V = 21, p = 0.03125, n = 6). Bottom panel: As above but for V2a-B neurons (Wilcoxon signed-rank test; FB, V = 2, p = 0.001953, n = 11; SB, V = 15, p = 0.0625, n = 5). Boxed plots are superimposed on trendlines from individual neurons. Note, 1 cell each for V2a-D and V2a-B slow subtypes behaved more like fast subtypes (dashed lines).

I) Top panel: Box plots of the maximum IPSC per cycle as a percentage of the maximum current (max IPSC%) for fast (FD, n = 7) and slow (SD, n = 7) V2a-Ds organized as in panel G. Bottom panel: As above but for fast (FB, n = 12) and slow (SB, n = 6) V2a-B neurons.

J) Top panel: Box plots of max IPSC% for fast and slow V2a-D neurons from panel *I*, collapsed into single slow (<35 Hz) and fast (>35 Hz) bins for purposes of for statistical analysis (Wilcoxon signed-rank test; FD, V = 0, p = 0.01563, n = 7; SD, V = 1, p = 0.03125, n = 7). Bottom panel: as above, but for fast and slow V2a-B neurons (Wilcoxon signed-rank test; FB, V = 0, p= 0.0004883, n = 12; SB, V = 4, p = 0.2188, n = 6).

K) Box plots of maximum excitatory and inhibitory current for FD (Wilcoxon signed-rank test; V = 0, p = 0.00781, n = 9 for excitation, n = 8 for inhibition) and SD (Wilcoxon signed-rank test; V = 0, p = 0.01563, n = 8 for excitation, n = 7 for inhibition) neurons.

L) As in *K* but for FB (V = 1, p = 0.0001221, n = 16 for excitation, n = 15 for inhibition) and SB (V = 0, p = 0.03125, n = 6 for excitation, n = 6 for inhibition) neurons.

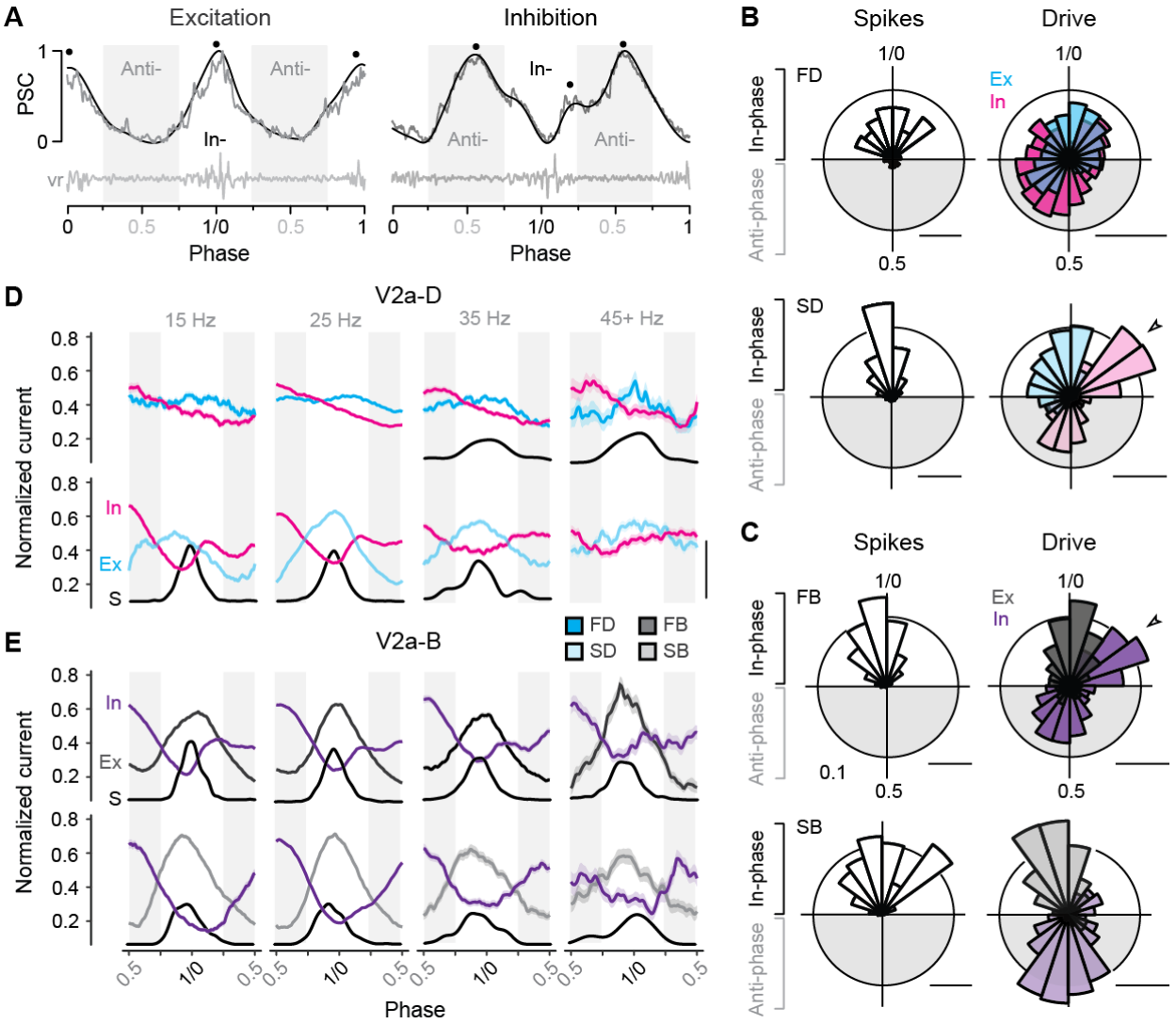

806 **Figure 6: Differences in timing of synaptic drive related to speed and V2a cell type**

807 **A)** Raw (grey) and low-pass filtered (black) traces of post-synaptic current (PSC), normalized to the peak
808 (1) and trough (0) of phasic excitation (left) and inhibition (right). Corresponding ventral root (vr) bursts
809 used to define in- and anti-phase (gray shaded boxes) currents are shown below. Block dots denote the
810 peaks identified by the findpeaks() function in MATLAB. Note, excitation has been inverted to simplify
811 comparisons to inhibition.

812 **B)** Left panel: Circular bar plots of spike phase for fast (FD, n = 9) and slow (SD, n = 8) V2a-D neurons.
813 Right panel: Circular bar plots of phase normalized peaks in low pass filtered EPSCs (FD, n = 9; SD, n =
814 7) and IPSCs (FD, n = 7; SD, n = 7). Arrowhead indicates prominent in-phase IPSC component for slow
815 V2a-Ds. Scale bars, 10% total distribution.

816 **C)** Left panel: Circular bar plots of spike phase for fast (FB, n = 16) and slow (SB, n = 6) V2a-B neurons.
817 Right panel: Circular bar plots of phase normalized peaks in low pass filtered EPSCs (FB, n = 11; SB, n =

818 6) and IPSCs (FB, n = 12; SB, n = 6). Arrowhead indicates prominent in-phase IPSC component for fast
819 V2a-bs. Scale bars, 10% total distribution.
820 **D)** Line plots from V2a-D neurons of averaged excitation (Ex; FD, n = 9; SD, n = 6), averaged inhibition
821 (In; FD, n = 7; SD, n = 7), and spike densities (S; FD, n = 7; SD, n = 7) broken into four ventral root burst
822 frequency (Hz) bins. Post synaptic current was normalized on a cycle-by-cycle basis, such that the
823 minimum and maximum current per cycle equaled 0 and 1 respectively. Scale bar for spike densities,
824 50% total distribution.
825 **E)** As in panel *D*, but averaged excitation (Ex; FB, n = 11; SB, n = 5), inhibition (In; FB, n = 12; SB, n = 6),
826 and spike densities (S; FB, n = 16; SB, n = 6) for V2a-B neurons.